Geosci. Instrum. Method. Data Syst. Discuss., 3, 31–58, 2013
www.geosci-instrum-method-data-syst-discuss.net/3/31/2013/
doi:10.5194/gid-3-31-2013

Geoscientific Instrumentation Methods and Data Systems
Discussions
Open Access

A radiation hardened digital fluxgate magnetometer for space applications

D. M. Miles[1], J. R. Bennest[2], I. R. Mann[1], and D. K. Millling[1]

[1]Department of Physics, University of Alberta, Edmonton, Alberta, T6G 2E1, Canada
[2]Bennest Enterprises Ltd., Summerland, British Columbia, V0H 1Z0, Canada

Received: 5 February 2013 – Accepted: 6 February 2013 – Published: 20 February 2013

Correspondence to: D. M. Miles (dmmiles@ualberta.ca)

Published by Copernicus Publications on behalf of the European Geosciences Union.

Abstract

Space-based measurements of the Earth's magnetic field are required to understand the plasma processes responsible for energizing particles in the Van Allen radiation belts and influencing space weather. This paper describes a prototype fluxgate magnetometer instrument developed for the proposed Canadian Space Agency (CSA) Outer Radiation Belt Injection, Transport, Acceleration and Loss Satellite (ORBITALS) mission and which has applications in other space and suborbital applications. The magnetometer is designed to survive and operate in the harsh environment of the Earth's radiation belts and measure low-frequency magnetic waves, the magnetic signatures of current systems, and the static background magnetic field. The new instrument offers improved science data compared to its predecessors through two key design changes: direct digitisation of the sensor and digital feedback combined with analog temperature compensation. These provide an increase in measurement bandwidth up to 450 Hz with the potential to extend to at least 1500 Hz. The instrument can resolve 8 pT on a 65 000 nT field with a magnetic noise of less than 10 pT per square–root Hz at 1 Hz. The prototype instrument was successfully tested and calibrated at the Natural Resources Canada Geomagnetics Laboratory showing that the mostly-digital design matches or exceeds its radiation-soft analog predecessor in sensitivity, noise, frequency range, and RMS accuracy.

1 Introduction and application

Space-based measurements of the Earth's magnetic field are required to understand the plasma processes underlying the solar-terrestrial connection. This includes the nature of the current systems and plasma waves during storms and substorms which are thought to cause acceleration and loss of energetic particles in the Van Allen radiation belts, and which constitute space weather. This paper describes a radiation hardened fluxgate magnetometer developed for the proposed Canadian Space Agency's Outer

Radiation Belt Injection, Transport, Acceleration and Loss Satellite (ORBITALS) mission (Mann et al., 2006).

The base fluxgate design used in this prototype has more than two decades of terrestrial heritage in the Canadian and American CARISMA/CANOPUS (Mann et al., 2008), POLARIS (Eaton et al., 2005), and EMScope/EarthScope USArray (Schultz, 2009) instruments built by Narod Geophysics Ltd (NGL) (e.g. Narod and Bennest, 1990). The NGL design was previously modified for low-radiation space applications as the Magnetic Field Instrument (MGF) in the CSA's Enhanced Polar Outflow Probe (ePOP) payload on the CAScade, Smallsat and IOnospheric Polar Explorer (CASSIOPE) satellite (Wallis et al., 2006).

Magnetic measurements for ORBITALS are technically challenging as the instrument must be capable of resolving small field variations in the presence of the large spin-tone signal caused by the satellite's spin (ten second period) in the frame of the Earth's magnetic field. These measurements must be made while surviving and operating within the Earth's radiation belts. In 2011, in addition to consideration for ORBITALS, the instrument development was continued for an additional application as a secondary science payload called Plasma and Radiation In Molniya Orbit (PRIMO) on the CSA's Polar Communications and Weather (PCW) satellite constellation (Trishchenko and Garand, 2012).

For both missions, the fluxgate magnetometer was required to measure the static magnetic field and magnetic waves at frequencies below 10 Hz. The static magnetic field measurements are required to understand the structure of the magnetospheric magnetic field, the role of current systems, and the dynamical motion and wave-particle acceleration, transport, and loss of energetic particles. Ultra Low Frequency (ULF) magnetic waves are thought to interact with low-energy particle populations and accelerate them to form damaging, high energy (MeV) space radiation (e.g. Friedel et al., 2002). Wave-particle interactions are also believed to be responsible for scattering particles into the loss cone. This depletes the radiation belts and has potentially important consequences for the atmosphere and climate change (e.g. Seppälä et al., 2007).

GID
3, 31–58, 2013

The prototype instrument uses only electronic components which have space grade (Class S) equivalents that are radiation tolerant to at least 100 krad. This allows the instrument to be manufactured for space flight applications in a high radiation environment. The new instrument has a low parts count and is not dependent on high-performance commercial components. This has been achieved by replacing much of the analog signal conditioning used in previous designs with equivalent digital processing in a Field Programmable Gate Array (FPGA).

The new design is simpler than its predecessors and offers improved science data through two key design improvements. Firstly, direct digitisation of the sensor removes the need for complex analog filtering of the fluxgate signal. Secondly, a novel dual pulse width modulation design provides digital feedback while preserving the sensor temperature compensation found in classical analog fluxgate magnetometers. These two changes provide bandwidth up to 450 Hz with the potential to extend to at least 1500 Hz in future work. This paper describes the instrument improvements, the key subsystems, and the performance of the resulting prototype instrument.

2 Instrument design

The instrument described in this paper is a redesign and further radiation hardened development of the Cassiope/ePOP fluxgate magnetometer instrument (MGF); analog signal conditioning circuitry was replaced with digital processing in an FPGA to mitigate radiation and temperature effects. The prototype uses a modified version of the flight-spare fluxgate sensor from the Cassiope/ePOP with two low-noise Infinetics ring-cores (Fig. 1). The ePOP MGF electronics were designed such that the noise floor of the overall instrument was set by the intrinsic noise of the two ring-cores in the sensor. One of the goals for the new prototype instrument was to achieve the same noise floor of less than 10 pT/$\sqrt{\text{Hz}}$ root-mean-square (RMS) at 1 Hz as was achieved by the Cassiope/ePOP fluxgate but in a radiation hard, digital, and temperature compensated design. As in the MGF instrument sensor, the $\boldsymbol{X}$ and $\boldsymbol{Y}$ components are derived from a single sense winding on each core while the Z component is derived from sense windings on each sensor core connected in series (see Fig. 2). The two dual-wound sensor bobbins are mounted on a block of MACOR machinable ceramic to minimise sensitivity changes due to temperature variation.

Figure 3 shows a single component block diagram of the new instrument. The prototype uses magnetic feedback to null the majority of the magnetic field inside the sensor. The measurement of the ambient field is then the sum of the applied magnetic feedback and the measured small residual field in the sensor. An FPGA controller generates a 28 800 Hz drive signal which is power amplified (PA) and sent into the drive winding to periodically saturate and unsaturate the ring cores. The direction of saturation is alternated to avoid magnetising the core. The modulated core permeability creates a fluxgate signal for each magnetometer component corresponding to the magnetic field strength inside the sensor in that axis. The current output from the sensor is converted to a voltage (I/V) and is sampled by the analog to digital converter (ADC) to become the input to a control loop implemented in the FPGA. The output of the control loop is sent to the digital to analog converter (DAC) and converted into a precise, temperature compensated current (V/I). This negative feedback drives each component of the magnetic field in the sensor head towards zero.

2.1 Direct digitisation

The bandpass filters and analog integrators traditionally used in second harmonic fluxgate magnetometers (e.g. Narod and Bennest, 1990) to sense the fluxgate signal at twice the sensor drive frequency ($2f$) are not required in this design. In the prototype, the sensor is directly digitised by sampling the instantaneous output from the sensor. In a classical design, the sensor is bandpass filtered, and integrated using analog processing before the signal is digitised. The direct digitisation approach can be described using the standard fluxgate induction equation (e.g. Ripka, 2001) which relates the sensor voltage V_i to the static magnetic $\boldsymbol{H}$-field through the modulation of the relative permeability μ_r of the sensor core:

$$V_i = (NA\mu_0\boldsymbol{H})\frac{\mathrm{d}\mu_r}{\mathrm{d}t}. \tag{1}$$

The sense coil is held in the short-circuit configuration shown in Fig. 4 using a virtual ground from the inverting input of an operational amplifier. The sense winding has a spike in sensitivity corresponding to the natural self-resonance of the coil. Holding the coil in a short-circuit linearises the coil response by suppressing this self-resonance. The voltage across the coil is forced to zero by the short circuit; however, there is still a circulating current determined by Ohms law.

The operational amplifier is configured as a transimpedance amplifier (i.e. a current to voltage converter). The capacitor C1 is selected such that it passes the second harmonic AC coupled fluxgate signal but blocks the quasi-static signal from the feedback DAC. Capacitor C2 ensures that the amplifier is stable. The output of the sensor and pre-amplifer can then be approximated as

$$V_{\mathrm{out}} = -\frac{R_1}{R_{\mathrm{winding}}}NA\mu_0\boldsymbol{H}\frac{\mathrm{d}\mu_r}{\mathrm{d}t}. \tag{2}$$

When the drive winding is modulating the relative permeability of the sensor ($\frac{\mathrm{d}\mu_r}{\mathrm{d}t} \neq 0$) the pre-amplifier produces a voltage V_{out}. This voltage is proportional to the instantaneous magnetic $\boldsymbol{H}$-field, has configurable gain via resistor R_1, and provides a low-impedance output which can be digitised without loading the sensor and distorting the signal.

The V_{out} signal is composed of the $\frac{\mathrm{d}\mu_r}{\mathrm{d}t}$ fluxgate action at the $2f$ frequency and the transformer coupled harmonics of the drive signal at f, $2f$, etc. The fluxgate action will cause V_{out} to pulse at $2f$ in proportion to the strength of the local magnetic field. However, these pulses will be superimposed on the constant, phase locked residual harmonics of the drive signal.

GID
3, 31–58, 2013

Figure 5 shows a time series of V_{out} under test conditions using applied external magnetic fields which are (a) large positive (+24,820 ± 10 nT), (b) small positive (+740 ± 10 nT), (c) near zero (−70 ± 10 nT), (d) small negative (−870 ± 10 nT), and (e) large negative (−24 430 ± 10 nT). The data was collected by disabling magnetic feedback, placing the sensor in a solenoid within a magnetic shield, and applying various magnetic field strengths ($\boldsymbol{B}$) using the solenoid and a precision current source. The vertical red lines in Fig. 5 show the times when the ADC samples V_{out}, phase locked to the $2f$ signal effectively creating a synchronous detector. The irregularity on the decreasing slope in Fig. 5a (+24 820 ± 10 nT) varies by axis and individual sensor. It is believed to be related to asymmetries in the sensor core.

The amplitude of the $2f$ pulses, as measured at the ADC trigger points, tracks the applied magnetic field in amplitude and polarity. However, even in a nearly zero field (Fig. 5c, −70 ± 10 nT), there is a residual AC signal from the drive current primarily at f and $2f$. The ADC measurements must be averaged over an even number of samples to cancel the harmonics. It is important to note that even in a strong field (Fig. 5a, +24 820 ± 10 nT and Fig. 5e, −24 430 ± 10 nT) the amplitude of the error signal at the ADC trigger points is monotonic and strictly increasing with magnetic field. This is essential because any local extrema or out-of-range polarity inversion would cause the control loop to apply feedback in the wrong direction.

2.2 Temperature compensated digital feedback

In this instrument, the pulse width modulation (PWM) based DAC changes its average output by varying the duty cycle of a pulse train emitted at a fixed repetition rate. A subsequent low-pass filter (LPF) attenuates the repetition-rate frequency, and its harmonics, leaving only the average value. The simplest possible PWM based DAC feedback system has three components:

GID
3, 31–58, 2013

1. A single-pole, double-throw (SPDT) break-before-make transmission-gate switch (sourced from precision bipolar reference voltages) to create a variable duty cycle pulse train.
2. A low-pass filter to remove the switching frequency.
3. A voltage to current converter to drive the feedback coil.

Some digital fluxgate magnetometers (e.g. O'Brien et al., 2007) omit the low-pass filter and simply drive the digital pulse train into the feedback coil using a resistor for current conversion. To first order, the resistor acts as a voltage to current converter. The average feedback current experienced by the sensor is the same and the input filters on the sensor pre-amplifier will generally remove the repetition rate signal.

However, a simple resistor is not a controlled current source and cannot be used to provide temperature compensation for the sensor. The geometry of the sensor's feedback winding will change slightly with temperature primarily due to variation in coil length. As a consequence, the amount of magnetic feedback for a given current varies with temperature. Acuña et al. (1978) describe a technique for temperature compensation by noting that the impedance of the coil also changes with temperature and that these two effects can be used to cancel each other.

In this prototype, a transconductance amplifier (i.e. voltage to current converter) is used to provide feedback current. However, it is intentionally unbalanced so that the voltage to current conversion factor depends on the coil impedance. This dependence on coil impedance is then tuned until the temperature effects of the coil impedance and the coil geometry are equal and opposite.

This temperature compensation technique has been widely used in analog fluxgate magnetometers (e.g. Narod and Bennest, 1990); however, it has been missing in previous digital designs. The technique requires a low-pass reconstruction filter on the digital feedback to avoid clipping the transconductance feedback amplifier with the comparatively large switching signal from the PWM. The design outlined below can be constructed from radiation hardened components and implements high resolution digital feedback while preserving the temperature compensation of the fluxgate sensor.

The feedback frequency range should generally be wide enough to include the sampling frequency to make the feedback control loop robust and stable. The prototype instrument measures each axis at 900 samples per second (sps). The PWM repetition rate was set a decade higher to allow a 3-pole low-pass reconstruction filter with −3 dB corner near 1 kHz to provide greater than 60 dB attenuation of the PWM repetition frequency. This leaves a residual PWM amplitude small enough to avoid saturating the feedback amplifier. The repetition rate of the PWM was set to 14 400 Hz (the next divisor of the common clock frequency) to ensure that the feedback is locked in phase with the other instrument functions.

The magnetic range of the instrument was set to ± 65 536 nT to cover the expected geomagnetic field experienced in ground and space applications. Resolving 8 pT within this range requires 24 bit resolution. The best available radiation hard ADC (the RAD1419) can provide 14 bits of resolution; however, two bits are lost accommodating the drive residuals for an effective 12 bits of resolution. This requires the remaining 12 bits of resolution to be supplied by the digital-to-analog converter in the feedback network. Note that although only 12 bits of resolution are required, the digital-to-analog converter must be quiet at the 24 bit level in the frequency range of the instrument to avoid being the dominant noise source in the error signal. In a PWM based digital-to-analog converter, this primarily involves suppressing the PWM repetition rate below the 24 bit level in the final data product.

The base frequency required for a simple PWM to deliver this would be:

$$14\,400\,\mathrm{Hz} \times 2^{12} = 58\,982\,400\,\mathrm{Hz} \approx 60\,\mathrm{MHz}. \tag{3}$$

This is significantly faster than the best available radiation hardened analog switches (Intersil part HS303ARH) which, in this prototype, started to have marginal performance at 20 MHz.

GID
3, 31–58, 2013

Figure 6 shows a functional diagram of a dual PWM feedback network which solves this problem. Each 10-bit PWM sets its output level by the duty cycle of the pulse train. The low-pass filter reduces the amplitude of the 14 400 Hz PWM signal. The voltage of the fine PWM is attenuated to set its scaling compared to the coarse PWM and provide two bits of overlap for the control system. The fine PWM is then summed with the coarse PWM to create a voltage that can be set with a $(10-2)+(10-2)=16$ bit resolution. Ultra-high stability, ultra-low temperature coefficient bulk foil resistors are used in the attenuator, summing network, and the transconductance amplifier feedback networks. The low-pass reconstruction filters do not completely suppress the 14 400 Hz repetition rate. However, the amplitude is small enough that a classical analog transconductance power amplifier can be used to convert the voltage output into a temperature compensated current source. This approach allows a radiation hardened implementation of both digital feedback and sensor temperature compensation.

3 Potential for high frequency measurements

The short-circuit coil and transimpedance amplifier topology used in the prototype is functionally equivalent to the pre-amplifier topology used by Primdahl et al. (1994) in a paper on high frequency fluxgate performance. In that paper, Primdahl used a more conventional digital switch synchronous detector and analog integrator; however, the functionality is very similar to that in this prototype digital instrument. Primdahl reported that the −3 dB point in the amplitude response of the instrument occurred at approximately 1500 Hz although this was tentatively attributed to the synchronous detector rather than the sensor or the fluxgate action.

Primdahl's results, and the fact that there is no obvious physical reason why the fluxgate action should decay with frequency, suggests that the AC response of the prototype instrument should be explored. The repetition rate of the feedback PWMs limits the prototype instrument to 900 samples per second or 450 Hz Nyquist. Testing

GID
3, 31–58, 2013

the performance of the instrument above this frequency therefore required probing the analog pre-amplifier signal directly.

The feedback network of the instrument was temporarily disabled by fixing both the coarse and fine PWM at mid-range. In this configuration, the error signal from the pre-amplifier is analogous to a standard amplitude modulated sinusoidal signal (cf. AM radio). The $2f$ signal replaces the carrier (frequency ω_c, amplitude A_c) and the applied magnetic field acts as the modulating signal (frequency ω_m, amplitude A_m). The result is a timeseries of the form:

$$y(t) = A_c \times \sin(\omega_c t) + \frac{A_m}{2}\left[\sin(\omega_c + \omega_m)t + \sin(\omega_c - \omega_m)t\right]. \quad (4)$$

This analogy allows us to visualise the fluxgate action directly by sampling the error signal with a bench-top spectrum analyser. The $2f$ carrier frequency shows as a spectral feature at 57 600 Hz whose amplitude is dependent on the static field strength. However, an applied AC test signal will appear as two sideband carriers at 57 600 Hz plus or minus the AC signal frequency. The panels in Fig. 7 show, from top to bottom, the resulting spectral plots for: no test signal, 100, 200, 500, 1000, and 1500 Hz. Note that the amplitude of the sideband carriers is constant with frequency up to 1500 Hz and there are no other large amplitude features within 57 600 ± 1500 Hz. This suggests that, if the PWM frequency and sampling frequency were increased, the prototype fluxgate should provide data up to at least 1500 Hz.

4 Instrument performance

4.1 Test setup

Magnetic noise and RMS error analysis were conducted at the National Resources Canada Geomagnetics Laboratory on Anderson Rd, Ottawa, ON, Canada. The Building 8 facility contains a calibrated reference source, a three-axis Helmholtz coil, and an observatory grade magnetometer to cancel local geomagnetic variations. This provides a magnetically quiet location suitable for the long-period measurements required to characterise the low-frequency noise floor of the instrument.

Instrument resolution and AC performance were completed at the University of Alberta CARISMA laboratory in Edmonton, AB, Canada. The fluxgate sensor was placed in a test solenoid within a three layer magnetic shield. The test signals were generated by driving the solenoid with a Stanford Research DS360 ultra low distortion function generator. This facility has significantly more magnetic noise than the NRCan facility and the test solenoid and signal generator are not calibrated against an established magnetic reference. However, the CARISMA laboratory test fixture was developed for testing induction coil magnetometers and is ideal for testing the dynamic performance of the prototype fluxgate.

4.2 Magnetic resolution

The prototype instrument is designed such that the analog-to-digital converter has a least significant bit of 57 pT. This is the smallest resolution which can accommodate the analog error signal under normal operating conditions. However, the error signal is digitized at 57 600 sps and decimated by 64 into a 900 sps data product. Oversampling by four times can create one effective bit of resolution. Therefore, oversampling by $N = 64 = 4^3$ creates three additional bits of resolution for an effective resolution of

$$\left\lceil \frac{\text{Physical Resolution}}{2^{\frac{\log N}{\log 4}}} \right\rceil = \left\lceil \frac{57\,\text{pT}}{2^3} \right\rceil = \left\lceil 7.1\,\text{pT} \right\rceil \tag{5}$$

or, to the next largest integer, 8 pT resolution. The instrument resolution was tested using a sinusoidal test signal applied by a solenoid within a three layer magnetic shield. Figures 8 and 9 show amplitude spectra resolving an 18 pT RMS (50 pT peak-to-peak) sine-wave test signals at 1 and 400 Hz, respectively. An 18 pT RMS test signal, rather than 8 pT RMS, was used such that the contribution of the noise floor to the spectral amplitude measurement was negligible. The narrow spectral features near 11, 55, and

60 Hz are believed to be environmental. The broad, low amplitude feature around 100 to 200 Hz is dependent on the DC power supply used and is believed to be instrumental due to poor power supply noise rejection.

The Effective Noise Bandwidth (ENBW) value shown in the Figs. 8 and 9 is the scaling factor, as defined by Heinzel et al. (2002), allowing the presented amplitude spectra to be converted into power spectral density via

$$\text{Amplitude Spectrum} = \sqrt{\text{Power Spectral Density} \times \text{ENBW}}. \tag{6}$$

4.3 Noise floor

Figure 10 shows a long period average power spectral density plot taken in the magnetically quiet NRCan environment. The prototype instrument resolves the the sub 10 pT/$\sqrt{\text{Hz}}$ RMS at 1 Hz noise of the sensor core and is consistent with the previous Cassiope ePOP MGF results. Significantly, the new digital design achieves the same noise floor and better resolution while providing 900 sps compared to 160 sps in the previous design. The double-peaked noise feature between 200 and 300 Hz is again believed to be related to the power-converter and will be addressed in the next revision of hardware.

4.4 RMS error

The RMS error of the instrument was measured over the full instrument range of ± 65 536 nT using 3-axis Helmholtz coils with main field compensation. Each measurement was averaged over 1 s to cancel the environmental 60 Hz noise. The prototype instrument has an RMS error of less than 7 nT over ± 65 536 nT or 0.005 % of full scale.

4.5 Performance summary

The key performance parameters of the prototype instrument are summarised in Table 1.

GID
3, 31–58, 2013

5 Future work

The current prototype was constructed from multiple printed circuit boards with wiring interconnects and significant debugging hardware. The next hardware iteration will be integrated into a single, flight ready card and the power consumption will be re-tested with the debugging tools removed. The instrument's power supply and the power supply rejection ratio will be improved to remove the double-peaked noise feature between 100 and 300 Hz seen in the amplitude and power spectral density plots. A faster analog switch or a third PWM on each component will be added to increase the speed of the digital feedback loop and the bandwidth of the instrument. Faster digital feedback may also require a more sophisticated control algorithm to allow the instrument to track very high slew rates such as those found on spinning sounding rocket applications which can be on the order of 5 Hz.

The prototype instrument is currently part of a proposed secondary plasma science payload on Canada's flagship Polar Communication and Weather (PCW) satellite constellation (Trishchenko and Garand, 2012). The instrument is also expected to be flown as a Canadian contribution to the fourth Norwegian Investigation of Cusp Irregularities (ICI-4) suborbital sounding rocket mission (Moen et al., 2003).

6 Conclusions

The prototype instrument delivers 8 pT resolution in a $\pm$ 65 536 nT field at 900 sps with a magnetic noise of less than 10 pT/$\sqrt{\text{Hz}}$ RMS at 1 Hz. The magnetometer is designed to be radiation tolerant to 100 krad and to be entirely constructed from space grade (Class S) parts so that it can be deployed in extreme radiation environments such as the Earth's radiation belts. The instrument uses a novel digital feedback process to improve the sampling rate and resolution while reducing complexity, parts count, and physical size. Significantly, the novel magnetic feedback design combines digital feedback with classic analog temperature compensation. This has produced a prototype

GID
3, 31–58, 2013

modern, digital fluxgate magnetometer suitable for a variety of ground, suborbital, and space applications.

Acknowledgements. This paper describes the improvement, extension and modernisation of an instrument design developed by Magnametrics, Narod Geophysics Ltd., and Bennest Enterprises Ltd. for the Cassiope/ePOP satellite. The University of Alberta, Department of Physics Electronics Shop provided significant assistance with the digital electronics. The authors would like to acknowledge the assistance of: David Barona, Bill Burris, Miroslaw Ciurzynski, Paul Davis, Alex Degeling, Andy Kale, Shengli Liu, Kyle Murphy, Barry Narod, Louis Ozeke, Jonathan Rae, Don Wallis, and Clare Watt. Instrument development was undertaken with the financial support of the Canadian Space Agency. I. R. Mann is supported by a Discovery Grant from the Canadian NSERC. The authors would like to thank Natural Resources Canada for the use of the Geomagnetics Laboratory facilities and their assistance characterizing and calibrating the instrument.

References

Acuña, M. H., Scearce, C. S., Seek, J., and Scheifele, J.: The MAGSAT vector magnetometer: A precision fluxgate magnetometer for the measurement of the geomagnetic field, Technical report, National Aeronautics and Space Administration, Goddard Space Flight Center, Greenbelt, Maryland, 1978. 38

Eaton, D. W., Adams, J., Asudeh, I., Atkinson, G. M., Bostock, M. G., Cassidy, J. F., Ferguson, I. J., Samson, C., Snyder, D. B., Tiampo, K. F., and Unsworth, M. J.: Investigating Canada's Lithosphere and earthquake hazards with portable arrays, EOS Transactions, 86, 169–173, 2005. 33

Friedel, R. H. W., Reeves, G. D., and Obara, T.: Relativistic electron dynamics in the inner magnetosphere – A review, J. Atmos. Sol.-Terr. Phys., 64, 265–282, 2002. 33

Heinzel, G., Rudiger, A., and Schilling, R.: Spectrum and spectral density estimation by the discrete fourier transform (DFT), including a comprehensive list of window functions and some new flat-top windows, Technical report, Max-Planck-Institut fur Gravitationsphysik, Teilinstitut Hannover, 2002. 43

GID
3, 31–58, 2013

Mann, I. R., Balmain, K. G., Blake, J. B., Boteler, D., Bourdarie, S., Clemmons, J. H., Dent, Z. C., Degeling, A. W., Fedosejeves, R., Fennell, J. F., Fraser, B. J., Green, J. C., Jordanova, V. K., Kale, A., Kistler, L. M., Knudsen, D. J., Lessard, M. R., Loto'aniu, T. M., Milling, D. K., O'Brien, T. P., Onsager, T. G., Ozeke, L. G., Rae, I. J., Rankin, R., Reeves, G. D., Ridley, A. J., Sofko, G. J., Summers, D., Thomson, I., Thorne, R. M., Tsui, Y. Y., Unick, C., Vassiliadis, D., Wygant, J. R., and Yau, A. W.: The outer radiation belt injection, transport, acceleration and loss satellite (ORBITALS): A Canadian small satellite mission for ILWS, Advances in Space Research, 38, 1838–1860, doi:10.1016/j.asr.2005.11.009, 2006. 33

Mann, I. R., Milling, D. K., Rae, I. J., Ozeke, L. O., Kale, A., Kale, Z., Murphy, K., Parent, A., Usanova, M., Pahud, D., Lee, E.-A., Amalraj, V., Wallis, D., Angelopoulos, V., Glassmeier, K.-H., Russell, C., Auster, H.-U., and Singer, H.: The upgraded CARISMA magnetometer array in the THEMIS era, Space Sci. Rev., 141, 413–451, doi:10.1007/s11214-008-9457-6, 2008. 33

Mann, I. R., Rae, I. J., Ozeke, L. G., Miles, D. M., Yau, A. W.: Plasma and Radiation In Molniya Orbit (PRIMO) Science Objective and User's Needs Definition Document, Technical report, Universities of Alberta and Calgary for the Canadian Space Agency, 2011.

Moen, J., Bekkeng, J. K., Pedersen, A., Aase, J. G., de Feraudy, H., Søraas, F., Blix, T. A., Lester, M., and Pryse, S. E.: ICI-1: a new sounding rocket concept to observe micro-scale physics in the cusp ionosphere, in: 16th ESA Symposium on European Rocket and Balloon Programmes and Related Research, 2–5 June 2003, Sankt Gallen, Switzerland, edited by: Warmbein, B., ESA Publications Division SP 530, Noordwijk, 543–548, 2003. 44

Narod, B. B. and Bennest, J. R.: Ring-core fluxgate magnetometers for use as observatory variometers, Phys. Earth Planet. Interior., 59, 23–28, doi:10.1016/0031-9201(90)90205-C, 1990. 33, 35, 38

O'Brien, H., Brown, P., Beek, T., Carr, C., Cupido, E., and Oddy, T.: A radiation tolerant digital fluxgate magnetometer, Meas. Sci. Technol., 18, 3645, doi:10.1088/0957-0233/18/11/050, 2007. 38

Primdahl, F., Nielsen, O., Petersen, J., and Ripka, P.: High frequency fluxgate sensor noise, Electron. Lett., 30, 481–482, 1994. 40

Ripka, P.: Magnetic Sensors and Magnetometers, Artech House, Inc., Northwood, MA, 2001. 35

Schultz, A.: EMScope: A continental scale magnetotelluric observatory and data discovery resource, Data Sci. J., 8, IGY6–IGY20, 2009. 33

Seppälä, A., Verronen, P. T., Clilverd, M. A., Randall, C. E., Tamminen, J., Sofieva, V., Backman, L., and Kyrölä, E.: Arctic and Antarctic polar winter NO_x and energetic particle precipitation in 2002–2006, Geophys. Res. Lett., 34, L12810, doi:10.1029/2007GL029733, 2007. 33

Trishchenko, A. P. and Garand, L.: Observing polar regions from space: advantages of a satellite system on a highly elliptical orbit versus a constellation of low Earth polar orbiters, Can. J. Remote Sens., 38, 12–24, 2012. 33, 44

Wallis, D. D., Narod, B. B., and Bennest, J. R.: The ePOP/CASSIOPE Magnetic Field Instrument, Proceedings of the 13th Canadian Astronautics Conference, ASTRO 2006, organized by CASI (Canadian Astronautics and Space Institute), 25–27 April 2006, Montreal, QC, Canada, 2006. 33

GID
3, 31–58, 2013

A radiation hardened digital fluxgate magnetometer

D. M. Miles et al.

Table 1. Performance summary of the prototype instrument.

Parameter	Current value
Resolution	8 pT
Cadence	900 sps
Noise floor	$< 10\ \mathrm{pT}/\sqrt{\mathrm{Hz}}$ at 1 Hz
RMS error	0.005 %
Potential radiation tolerance	100 krad
Power	1.5 W
Electronics dimensions	150 × 150 × 30 mm

GID
3, 31–58, 2013

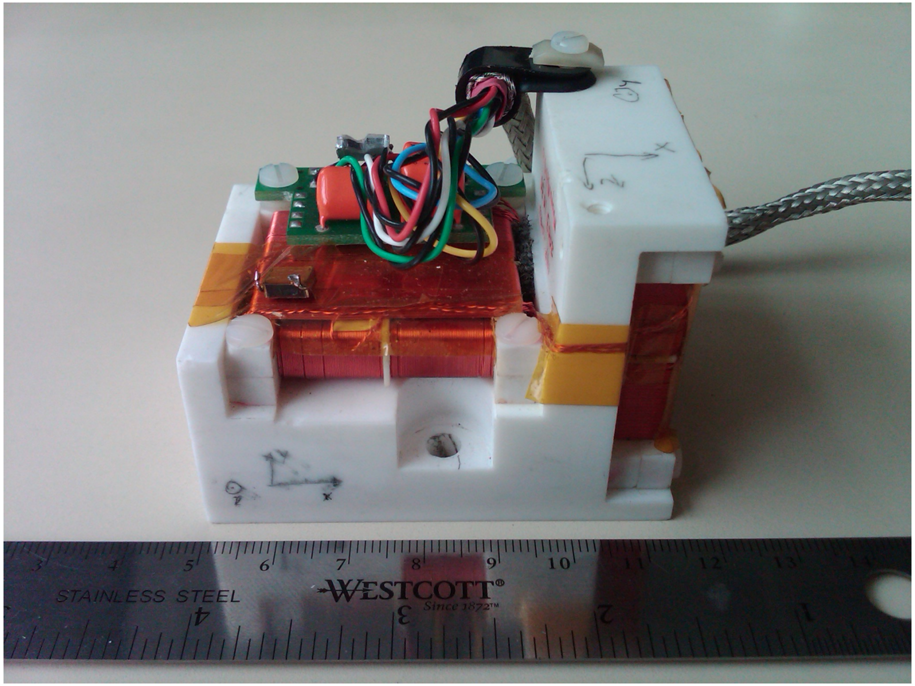

Fig. 1. Fluxgate sensor used in the prototype instrument. This hardware is the Cassiope/ePOP MGF engineering model with minor modifications.

GID
3, 31–58, 2013

A radiation hardened digital fluxgate magnetometer

D. M. Miles et al.

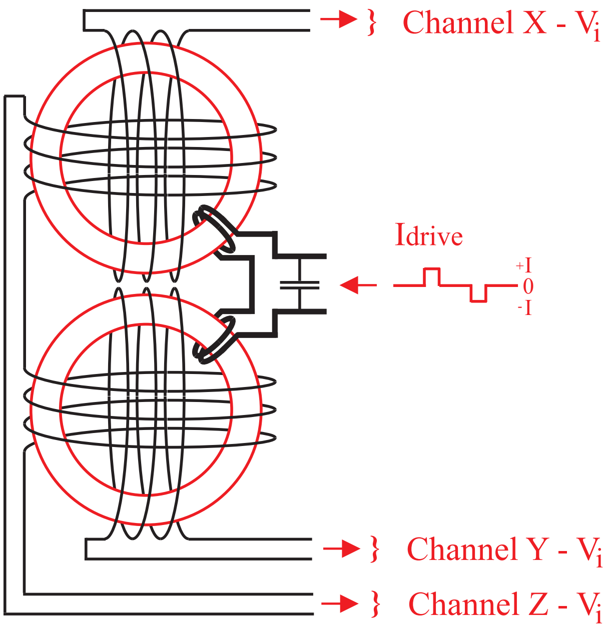

Fig. 2. Schematic wiring of the ***X***, ***Y***, and ***Z*** sensor components and the drive winding in the prototype. ***X*** and ***Y*** are single windings while ***Z*** is derived from two windings in series. Note that the two ring-cores are physically orthogonal as shown in Fig. 1.

GID
3, 31–58, 2013

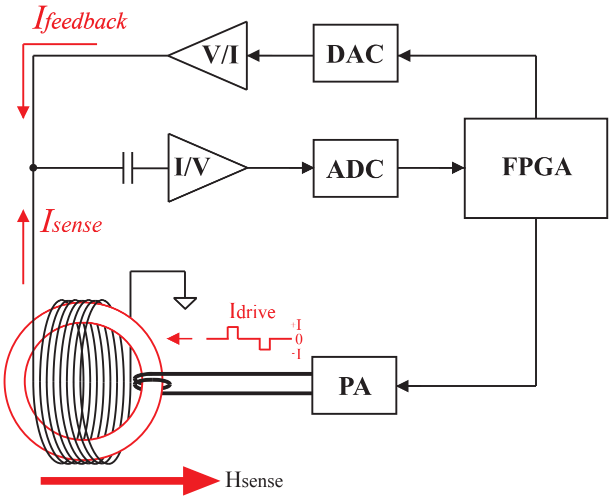

Fig. 3. Schematic of one fluxgate component showing the major components. The FPGA controller generates a 28 800 Hz drive signal that is power amplified (PA) and sent into the drive winding to periodically saturate and and unsaturate the ring cores. The bandpass, phase synchronous detector, low-pass, and integrator hardware in a classic 2 *f* fluxgate are replaced with a current to voltage converter (I/V) and an ADC to digitize the signal. An FPGA uses the fluxgate signal as the input to a control loop to drive the magnetic field in the sensor towards zero. The output of the control loop is converted to an analog signal (DAC) and then to a high-precision, temperature compensated current to provide magnetic feedback (V/I).

GID
3, 31–58, 2013

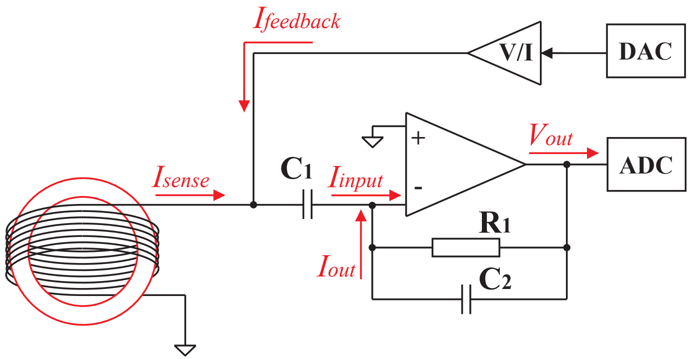

Fig. 4. Equivalent circuit of the sensor pre-amplifier in the prototype instrument.

GID
3, 31–58, 2013

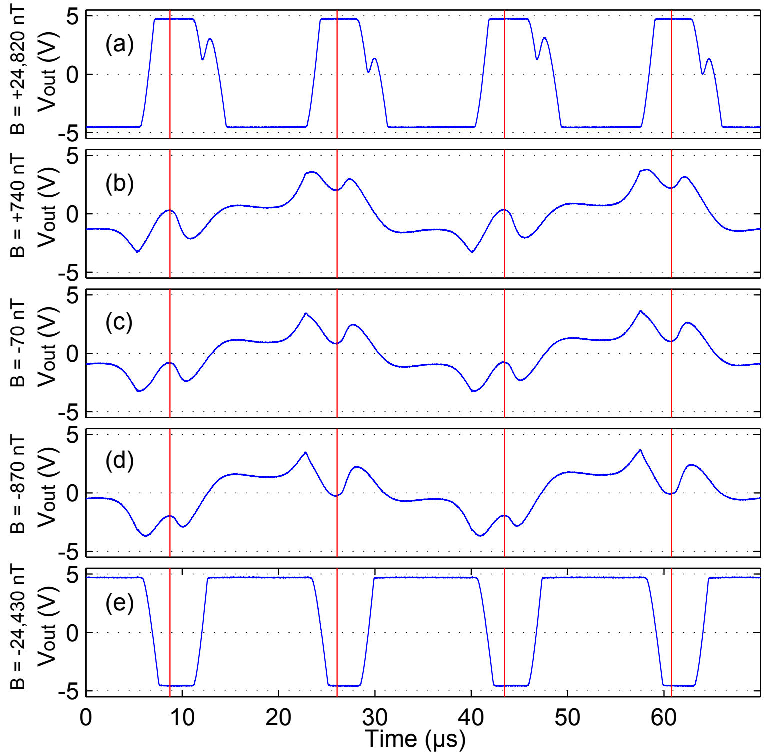

Fig. 5. V_{out} at various applied magnetic field that are **(a)** large positive (+24 820 ± 10 nT), **(b)** small positive (+740 ± 10 nT), **(c)** near zero (−70 ± 10 nT), **(d)** small negative (−870 ± 10 nT), and **(e)** large negative (−24 430 ± 10 nT).

GID
3, 31–58, 2013

A radiation hardened digital fluxgate magnetometer

D. M. Miles et al.

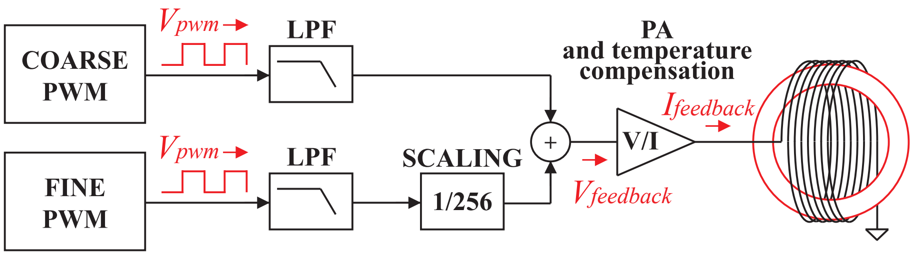

Fig. 6. Block diagram of the dual pulse width modulation feedback network of the prototype instrument. The output is built up from two 10 bit PWMs at 14 400 Hz and low-pass filtered at 1 kHz. The two PWMs are scaled to overlap by two bits, summed, and converted into a feedback current using an intentionally mis-balanced transconductance amplifier to temperature compensate the feedback coil.

GID
3, 31–58, 2013

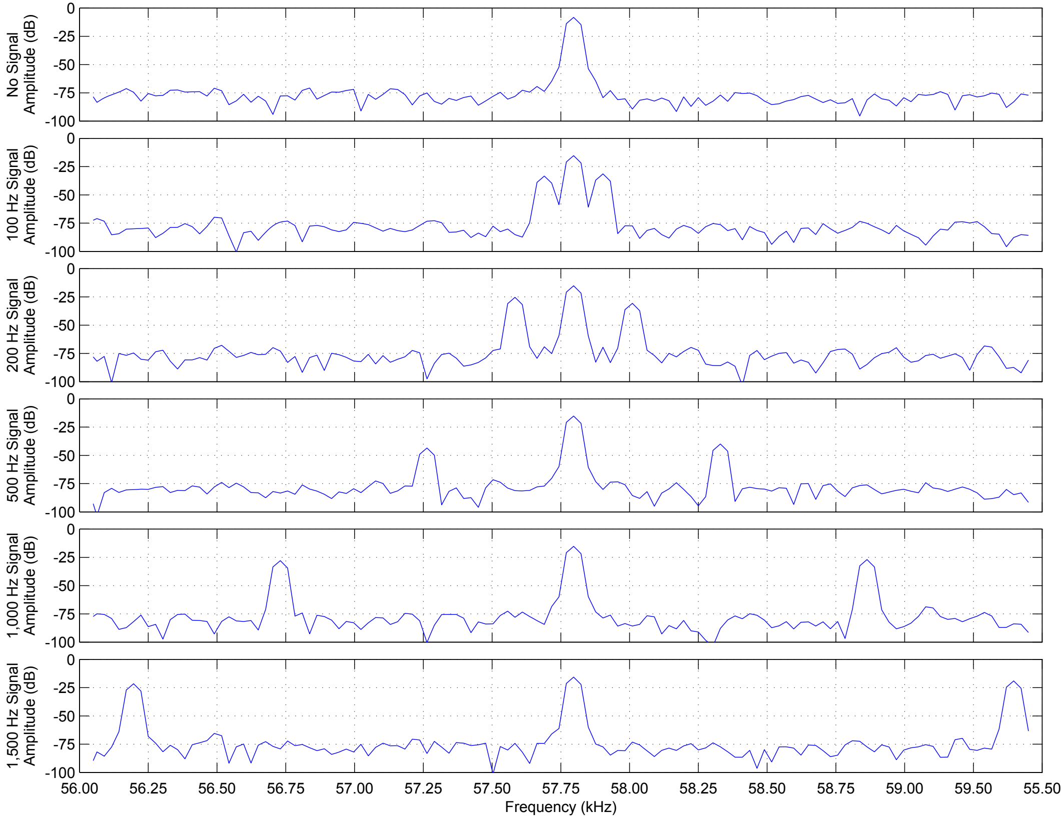

Fig. 7. Spectral analysis of the directly sampled error signal showing the modulation of the 2 *f* major carrier sidebands by applied sinusoidal magnetic signals up to 1500 Hz.

GID
3, 31–58, 2013

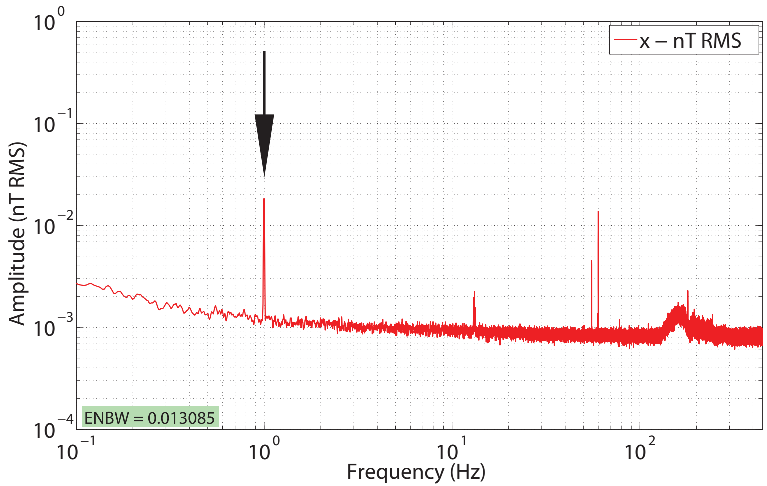

Fig. 8. Amplitude spectrum showing resolution of prototype instrument. Arrow shows a 18 pT RMS sinusoidal test signal at 1 Hz.

GID
3, 31–58, 2013

A radiation hardened digital fluxgate magnetometer

D. M. Miles et al.

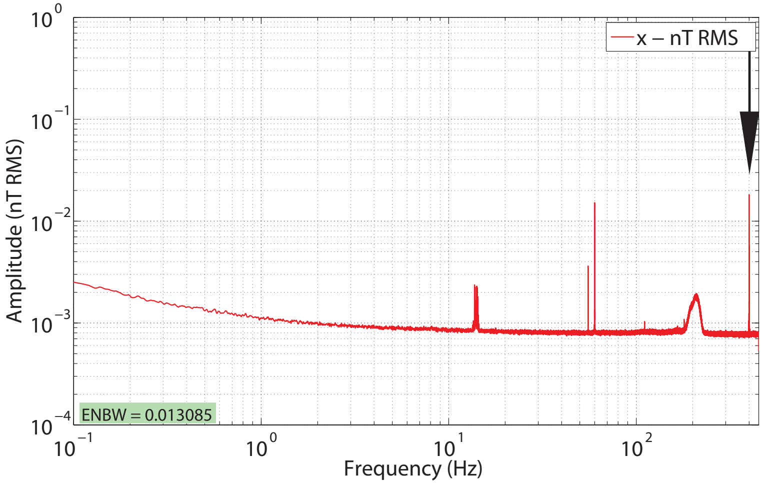

Fig. 9. Amplitude spectrum showing resolution of prototype instrument. Arrow shows a 18 pT RMS sinusoidal test signal at 400 Hz.

GID
3, 31–58, 2013

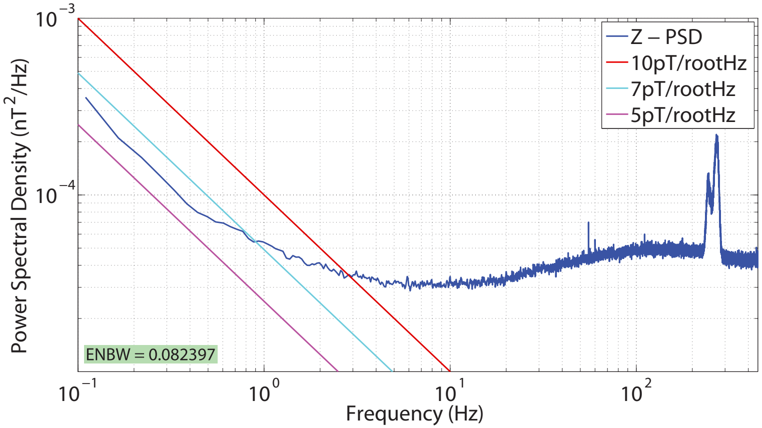

Fig. 10. Power spectral density noise floor of the prototype instrument.

GID
3, 31–58, 2013

A radiation hardened digital fluxgate magnetometer

D. M. Miles et al.